

Hilbert space fragmentation in a frustration-free fully packed loop model

Zhao Zhang^{1,2,*} and Henrik Schou Røising^{2,3,†}

¹*SISSA and INFN, Sezione di Trieste, via Bonomea 265, I-34136, Trieste, Italy*

²*Nordita, KTH Royal Institute of Technology and Stockholm University,*

Hannes Alfvéns väg 12, SE-106 91 Stockholm, Sweden

³*Niels Bohr Institute, University of Copenhagen, Jagtvej 128, DK-2200 Copenhagen, Denmark*

(Dated: June 10, 2022)

We consider a quantum fully packed loop model on the square lattice with a frustration-free projector Hamiltonian and ring-exchange interactions acting on plaquettes. A boundary Hamiltonian is added to favour domain-wall boundary conditions and link ground state properties to the combinatorics and six-vertex model literature. We discuss how the boundary term fractures the Hilbert space into Krylov subspaces, and we prove that the Hamiltonian is ergodic within each subspace, leading to a series of energy-equidistant exact eigenstates in the lower end of the spectrum. Among them we systematically classify both finitely entangled eigenstates and product eigenstates. Using an exact recursion relation and the enumeration of half-plane fully packed loop configurations with varying boundary configurations on one side, we perform a numerically exact lattice calculation of the ground state bipartite entanglement entropy, yielding area law scaling. Finally, the spectrum is shown to be gapless in the thermodynamic limit with a trial wave function constructed by adding a twist to the ground state superposition.

I. INTRODUCTION

Ergodicity and its breaking lies at the foundation of modern statistical mechanics. It plays a key role in understanding of why the long-time average of an observable of a single system can be well-approximated by a statistical ensemble average. In quantum systems, any initial state being thermalized necessarily requires each eigenstate of the Hamiltonian to be thermalized, leading to the so-called eigenstate thermalization hypothesis (ETH) [1, 2]. Over the past few years, ETH violation has been realized outside the scope of the integrability and many-body localization paradigms [3, 4], such as in quantum many-body scars (QMBSs) and Hilbert space fragmentation [4, 5].

Two types of models have played important roles in understanding these novel mechanisms of weak ergodicity-breaking. The first type is kinetically constrained models, which can arise as low energy effective models through a Schrieffer–Wolf transformation [6, 7]. The dimensionality of constrained Hilbert spaces typically grows as an integer sequence, reflecting an underlying combinatorial structure. In one dimension, a prime example is the PXP model [8–10], which successfully explains Rydberg blockade experiments [11]. The dimensionality of its Hilbert space grows as the Fibonacci numbers with the asymptotic scaling 1.618^N . In two dimensions, arguably one of the most studied models in classical statistical mechanics and combinatorics is the six-vertex model. With periodic boundary conditions, its Hilbert space dimension grows as 1.540^{N^2} , following from Lieb’s solution to the square ice problem [12]. Sophisticated

results have been established when the model is subject to domain-wall boundary conditions (DWBCs), for which a bijection between configurations and alternating sign matrices (ASMs) [13] has been proven. The exact enumeration of ASMs is a celebrated result in combinatorics [13–16]. Notably, progress has also been made in technologies and ideas for realizing classical and quantum spin ice models [17], with platforms ranging from arrays of ferromagnetic islands [18] to two-dimensional Rydberg atom arrays [19–23].

Instead of enforcing a hard Hilbert space constraint as a high-energy penalty, one can also introduce order-one terms in the Hamiltonian to yield the ground state as the superposition of states from the (classical) configuration space of some combinatorial problem. This is done with frustration-free (FF) Hamiltonians, the ground state of which is the simultaneous lowest energy eigenstate of all its local terms. Examples of frustration-free models in 1D include the Motzkin [24] and the Fredkin spin chain [25, 26], for which ground state configurations reassemble combinatorial structures known as Motzkin and Dyck walks. Recently, it has been shown that by flipping the signs of some of the projectors, the FF eigenstate can be relocated to the middle of the spectrum, making it qualified for a quantum many-body scar. These systems, as well as the original models, also exhibit Hilbert space fragmentation [27–29], which refers to the emergence of exponentially many dynamically disconnected subspaces.

Another permeable theme in quantum many-body physics is entanglement entropy (EE), not only because it is a unique feature of the quantum world, but also due its crucial role in building efficient numerical algorithms and in the understanding phenomena ranging from black holes to topological order. While a generic eigenstate in the Hilbert space have been shown to have volume-law EE [30], the EE of ground states of local and gapped Hamiltonians generally obey an area law, $S \sim N^{d-1}$,

* zz8py@virginia.edu

† henrik.roising@nbi.ku.dk

where d is the spatial dimension. A milestone in the study of EE has been Hastings' rigorous proof of area law in gapped one-dimensional (1D) systems [31]. Recently, a similar result in two dimensions (2D) has been proven for frustration-free models [32, 33]. While area law is ubiquitous in gapped systems, plenty of examples of area law violation have been found in gapless systems. In (1+1)-dimensional critical systems described by a conformal field theory the EE has a logarithmic scaling [34], and the EE of free fermions scales as $N^{d-1} \ln N$ [35]. In 1D the aforementioned Motzkin and Fredkin spin chains violate the area law even more strongly, with up to volume-law scaling [36–39]. Despite the plethora of 1D lattice models, their 2D counterparts are yet to be discovered.

A crucial ingredient of the Motzkin and Fredkin models is that they allow a height representation that is able to carry non-local information of the interactions. The first obstacle in generalizing this to 2D is to find a well-defined height function that does not give rise to any ambiguity when going around a closed loop in the lattice. This problem is intrinsically avoided in the context of dimer and fully packed loop (FPL) models [40–43]. To further enforce the incremental height change between adjacent plaquettes to be ± 1 on square lattice, we opt for FPLs.

The paper is organised as follows. In Sec. II, we introduce the Hilbert space and Hamiltonian of our model. In Sec. III we explore ergodicity breaking and Hilbert space fragmentation in detail (Sec. III A), in addition to constructing a series of exact eigenstates (Sec. III B). In Sec. IV we compute numerically the exact ground state bipartite entanglement entropy between half-systems, yielding area law scaling. In Sec. V we construct a trial wave function with vanishing energy in the thermodynamic limit, demonstrating that the model is gapless. Finally, we provide a summary and propose future directions.

II. THE MODEL AND ITS DUAL LATTICE FORMULATION

We consider a square lattice G of $N \times N$ vertices, with binary degrees of freedom living on the horizontal and vertical bonds connecting neighbouring vertices. We constrain the Hilbert space to that of the fully packed loop (or 2-dimer) coverings of the lattice by the diagonal Hamiltonian $H_0 = V \sum_{i,j=1}^N (\sigma_v(i,j) + \sigma_h(i,j) + \sigma_v(i,j+1) + \sigma_h(i+1,j))^2$, where subscripts v and h refer to vertical and horizontal bonds respectively, and $\sigma = +1$ ($\sigma = -1$) for a covered (uncovered) bond. In the limit $V \gg 1$ we can effectively work in the ground state manifold of H_0 . In the constrained Hilbert space we consider the low-energy effective Hamiltonian

$$H = H_{\text{bulk}} + H_{\partial} = \sum_{p \in \text{bulk}} P_p + H_{\partial}, \quad (1)$$

$$P_p = \frac{1}{2} \left(\left| \begin{array}{c} \uparrow \downarrow \\ \downarrow \uparrow \end{array} \right\rangle - \left| \begin{array}{c} \downarrow \uparrow \\ \uparrow \downarrow \end{array} \right\rangle \right) \left(\left\langle \begin{array}{c} \uparrow \downarrow \\ \downarrow \uparrow \end{array} \right| - \left\langle \begin{array}{c} \downarrow \uparrow \\ \uparrow \downarrow \end{array} \right| \right)_p.$$

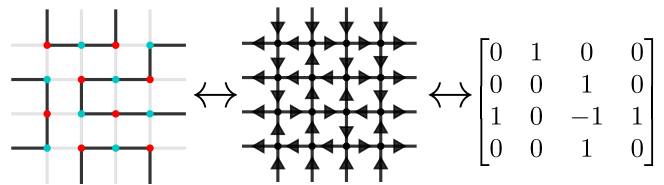


FIG. 1. Bijections with domain-wall boundary conditions. Left: fully packed loop configuration, middle: six-vertex model configuration, right: alternating sign matrix. The mapping between the first two representations is explained in Fig. 2 (a), and the mapping between the latter two amounts to assigning a and b vertices to 0, and c vertices to ± 1 [44].

The Rokhsar–Kivelson projectors, P_p , contain a diagonal potential term and an off-diagonal ring-exchange kinetic term that allows parallel covered bonds to resonate [45]. Here bonds are either covered (black) or uncovered (light gray), with the bond-spin conversion rules in Fig. 2 (b). The sum above runs over the bulk plaquettes, which there are $(N-1)^2$ of. The boundary terms

$$H_{\partial} = H_{\partial}^t + H_{\partial}^b + H_{\partial}^l + H_{\partial}^r + 2N,$$

$$H_{\partial}^t = \sum_{x=1}^N (-1)^x \left| \downarrow \right\rangle \left\langle \downarrow \right|_{x,N},$$

$$H_{\partial}^b = \sum_{x=1}^N (-1)^{x+1} \left| \uparrow \right\rangle \left\langle \uparrow \right|_{x,1} \quad (2)$$

$$H_{\partial}^l = \sum_{y=1}^N (-1)^y \left| \rightarrow \right\rangle \left\langle \rightarrow \right|_{1,y},$$

$$H_{\partial}^r = \sum_{y=1}^N (-1)^{y+1} \left| \leftarrow \right\rangle \left\langle \leftarrow \right|_{N,y}.$$

impose a domain-wall boundary condition (labelled DWBC1) on the ground state, where every other bond is covered along the boundary (see Fig. 2 (c)). Above, subscripts denote the (horizontal or vertical) bond position (x, y) , as counted from the lower left of the graph with row-major ordering. With these boundary conditions FPL coverings are also in bijection to alternating sign matrices [46], see Fig. 1.

The bulk Hamiltonian has the apparent \mathbb{Z}_2 symmetry \mathcal{R} of reversing the covering of all the bonds, satisfying

$$[H_{\text{bulk}}, \mathcal{R}] = 0, \quad (3)$$

which is broken by the boundary terms,

$$\{H_{\partial}, \mathcal{R}\} = 4N\mathcal{R}. \quad (4)$$

The full Hamiltonian also has a hidden symmetry given by Wieland's gyration [47], which reverses the coverings around only the non-flippable plaquettes, while leaving the flippable ones unchanged.

The off-diagonal terms in Eq. (1) relate FPL configurations differing on a single plaquette with parallel bonds

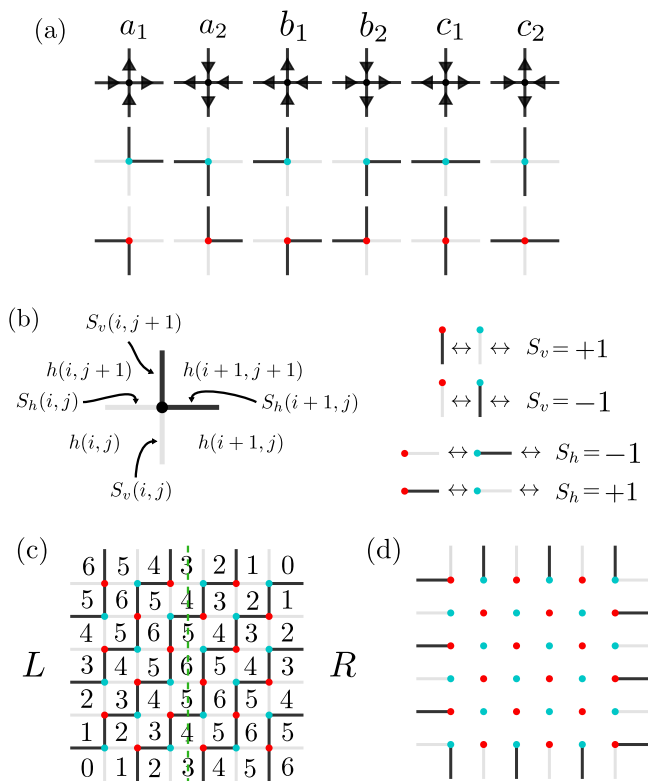


FIG. 2. (a) Mapping between configurations of the six-vertex model (top row) and fully packed loop configurations (FPLs, lower two rows), with rules alternating on the even (cyan dots) and odd (red dots) sublattices [44]. (b) Height (on plaquettes) and spin (on bonds) representation of FPLs, which are related as $\vec{S} = (S_v, S_h) = \vec{\nabla}h$ with discrete derivatives, see the main text. The FPL constraint amounts to imposing $\vec{\nabla} \times \vec{S} = 0$ around each vertex. (c) Maximal height configuration for $N = 6$ with domain-wall boundary condition DWBC1 in the height representation. The dashed green line represents the cut between the left (L) and right (R) half-systems of which we calculate the ground state entanglement entropy in Sec. IV. (d) Boundary conditions labelled DWBC2 relevant for the unique and exact excited state with energy $E = 4N$ described in Sec. III B.

covered in different directions. This is conveniently expressed in the height representation on the dual lattice [40, 42]. On the square lattice the height field is integer-valued and changes in units of ± 1 between neighbouring plaquettes. Using the bipartite rules summarized in Fig. 2 (b) the conversion between spins and height is compactly expressed as $\vec{S} = (S_v, S_h) = \vec{\nabla}h$, with $\partial_x h(i, j) := h(i+1, j) - h(i, j)$ and $\partial_y h(i, j) := h(i, j+1) - h(i, j)$. The FPL constraint then amounts to imposing $\vec{\nabla} \times \vec{S}(i, j) = 0$ around each vertex. It can easily be verified that these definitions make precisely the (flipable) plaquettes with two parallel covered bonds local extrema in the height, see Fig. 3.

On the dual lattice, the model can be expressed as the

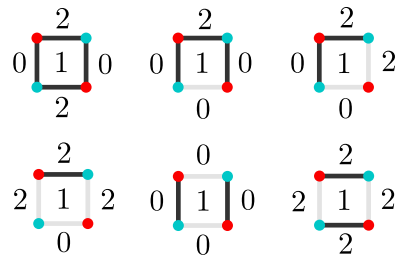


FIG. 3. Flippable plaquettes are precisely those for which the height is above or below all its four neighbours.

kinetically constrained Hamiltonian

$$H^* = \sum_{p \in \text{bulk}} (\Pi_p^> + \Pi_p^< - \Pi_p^> h_p^+ \Pi_p^< - \Pi_p^< h_p^- \Pi_p^>) + H_{\partial}^*, \quad (5)$$

where $\Pi_p^{>(<)}$ projects onto the state where the four neighboring plaquettes of p all have the same height above (resp. below) the height of p , and $h_p^{+(-)}$ increases (resp. decreases) the height of plaquette p by 2. The boundary term is given by

$$H_{\partial}^* = h(1, 1) - h(1, N+1) - h(N+1, 1) + h(N+1, N+1) + 2N. \quad (6)$$

The height representation on the dual lattice reveals another symmetry of the Hamiltonian. The accumulated height along each row $\sum_{j=1}^N S_v(i, j)$ or column $\sum_{i=1}^N S_h(i, j)$, or any other path connecting two boundary plaquettes, is conserved. Although these are not all independent conserved charges, the number of conserved charges grows exponentially in system size, which is fundamentally different from the one-dimensional case, like in the Heisenberg spin chain where only the total magnetization is conserved. This leads to a new mechanism of Hilbert space fragmentation, to be discussed in the next section.

III. HILBERT SPACE FRAGMENTATION AND EXACT EIGENSTATES

In the absence of kinetic terms on the boundary, the Hilbert space is fragmented into exponentially many Krylov subspaces which are not connected by the bulk Hamiltonian. In Appendix A we prove that the bulk Hamiltonian is ergodic within each Krylov subspace spanned by all the FPL configurations sharing the same boundary configuration. In this section we identify exact unentangled and finitely entangled eigenstates, by making simple observations of constraints on the boundary configurations. Among the exact eigenstates we construct the exact and unique ground state and its twin ceiling state.

A. Product eigenstates and finitely entangled eigenstates

If we follow the height counter-clockwise around the perimeter, the fact that it must come back to the same value after a full cycle implies that there must be at least one pair of height kink and anti-kink along the graph perimeter. Moreover, if anywhere on the lattice, there is a strip in which the height changes monotonically, and which has a right-angle turn, the height in the entire rectangle spanned by the two perpendicular sides must also change monotonically between diametrically opposing corners of the rectangle. We will henceforward refer to this as the “*convexity lemma*”, and use it repetitively. The key point is that since flippable plaquettes correspond to local extrema in the height, a monotonic segment can not contain any flippable plaquettes.

An immediate consequence of the convexity lemma is that a monotonic segment on the perimeter cannot cover two corners. Thus, besides the special case of two kinks being located on diagonally opposing corners as described below, there must be at least two pairs of alternating kink and anti-kink, with the sum of lengths of every other segment being $2N$. A four-segment case is depicted in Fig. 4.

As for the exceptional kink-antikink case, the height change must be monotonic in each row and column inside the bulk, so there are no flippable plaquettes in this case. We have thus found the first product eigenstate, as depicted in Fig. 5 (a) (for which the kink and the anti-kink are located at diagonally opposing corners). With two kink-antikink pairs, it is still easy to pick boundary configurations that only allow one bulk configuration. First, notice that the only way in which none of the four segments go around a corner is for each of them to cover exactly one side of the lattice. This gives the ground state boundary configuration depicted in Fig. 2 (c). Otherwise, each segment must go around one corner and one corner only.

If the four rectangles formed by the four monotonic segments cover the entire square lattice, it also results in a product eigenstate. This gives the states shown in Fig. 5 (b), (c), and (d). Together, up to translations and rotations, they exhaust all product eigenstates with two pairs kink-antikink on the boundary. This can be seen by writing each segment length as $l_i = x_i + y_i$ for $i = 1, \dots, 4$, see Fig. 4. Then the constraint $\min(x_1 + x_3, y_1 + y_3) \leq N - 1$ and $\min(x_2 + x_4, y_2 + y_4) \leq N - 1$ can only be satisfied if the minima are either N or $N - 1$, as their sums are always $2N$. The former gives (b) and (c), up to translations, and the latter gives (d), up to translations and $\frac{\pi}{2}$ rotations.

By now it can be seen that in general, a rule in searching boundary configurations yielding product eigenstates is that each plaquette in the lattice is penetrated by at least one height gradient line. Here gradient line just means any directed path (among multiple choices) along which the height changes monotonically and should not

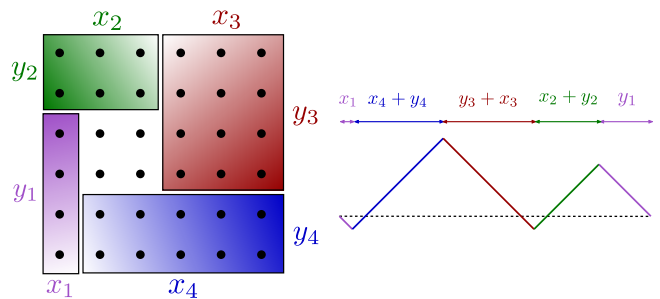


FIG. 4. A boundary configuration with four monotonic segments (two kinks and two anti-kinks), demanding four rectangular monotonic regions near four corners, leaving a core with a single flippable plaquette. The right panel shows the corresponding height going around the lattice boundary counter-clockwise.

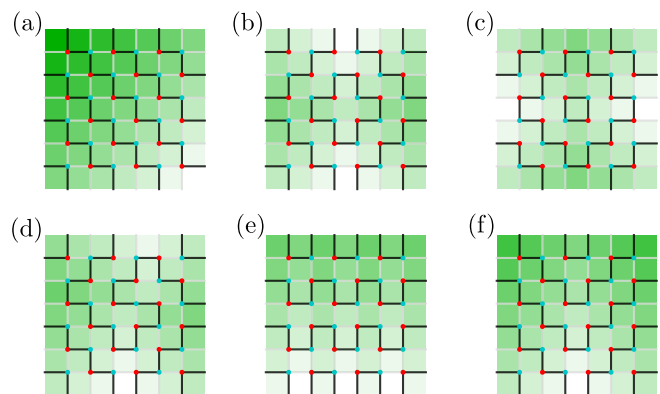


FIG. 5. Representatives of the two types of product eigenstates in isolated one-dimensional Krylov subspaces, with the opaque green color scale reflecting the height. (a), (e), and (f) have straight height gradient lines penetrating to opposite sides of the lattice, while (b), (c), and (d) have a saddle point of height gradients in the bulk. The energy of (a), (b), (c), (e), (f) is always $2N$, while the energy of (d) is $2N - 2$. Up to translations and rotations, the only remaining product states not depicted here have height functions being monotonic in one direction, and globally shifted parallel random walks in the orthogonal direction.

be confused with the direction of steepest descent. Gradient lines must start and end at boundaries, as loops are not allowed in the bulk, and endpoints imply a flippable plaquette. We now prove that the only possible full coverage of gradient lines, other than the special ones going around four corners as we discussed above, are parallel straight line coverings, corresponding to product states of the type Fig. 5 (e) and (f).

If there is at least one plaquette being traversed by a gradient line that starts and ends on opposite sides, we call this plaquette (i, j) , otherwise, it has to belong to one of the cases studied before. We start with a plaquette (i, j) in the bulk. Assume that it is traversed by a gradient line starting from side a and ending on side b . We examine the case where a and b are opposite sides,

and that where they are adjacent ones, respectively. In the first case case, without loss of generality, assume the coordinates of the two end points are $(i_a, 1)$ and (i_b, N) , with $i_a \leq i \leq i_b$. Then we immediately have that the entire region between i_a and i_b is traversed by straight gradient lines from the bottom to the top of the lattice, by the convexity lemma. But the outside lines will have nowhere to go except turning to the adjacent side, resulting in either a curl or violation of the convexity lemma.

If however, all gradient lines turn to end on adjacent sides, an analogous argument will result in product states of the type in Fig. 5 (b), (c) or (d). Hence we have exhausted all the possible unentangled eigenstates. Alternatively, the above argument can be made elegantly in the six-vertex language. In fact, much all the above argument could have been bought by those who are comfortable enough to embrace a discrete version of electrostatics, meaning gradient lines are necessarily curl-free, and source-free if unflippable. It is then clear that the cases in Fig. 5 are the only possible distributions avoiding sources or drains.

Apart from product eigenstates, the lowest entangled frustration-free eigenstate corresponding to the boundary configuration in Fig. 4, which is a equal superposition of two FPLs differing only by the center plaquette, with EE of $\ln 2$. One can further explicitly diagonalize a 2×2 plaquette system subject to DWBC, which is satisfied by the four-plaquette core surrounded by four monotonic rectangular wings. These states have area law entanglement entropy of the size of the core, which can be anywhere between 1 and N , if the cut is through it.

B. Exact eigenstates

As we prove in Appendix A, each consistent boundary configuration forms a Krylov subspace, in which a uniform superposition of all FPLs with that boundary configuration is an eigenstate. Among these would-be degenerate eigenstates, the boundary Hamiltonian picks the one with DWBC1 to be the unique and global ground state

$$|\text{GS}\rangle = \frac{1}{\sqrt{A(N)}} \sum_{\mathcal{F} \in \text{FPL with DWBC1}} |\mathcal{F}\rangle, \quad (7)$$

where the normalization constant

$$A(N) = \prod_{m=0}^{N-1} \frac{(3m+1)!}{(N+m)!}, \quad (8)$$

is equal to the number of ASMs [48] due to the domain-wall boundary conditions realized by the ground state [13–16], cf. Fig. 1.

It is possible to do a q -deformation to plaquette operators $P_p(q) = \frac{1}{1+q^2} (|\uparrow\uparrow\rangle - q|\uparrow\downarrow\rangle) (|\downarrow\uparrow\rangle - q|\downarrow\downarrow\rangle)_p$ to get a volume weighted ground state. Configurations differing only at a single plaquette come in pairs with a ratio of

weights q between the configurations with vertically and horizontally oriented bonds. This means that the configurations in the sum of Eq. (7) would acquire weights of $q^{\frac{1}{2}V(\mathcal{F})}$, where $V(\mathcal{F})$ is the sum of the heights on each plaquette in \mathcal{F} . In the limit of $q \rightarrow \infty$ (resp. $q \rightarrow 0$), we expect anisotropic configurations with the covered bonds forming a bottom-left to top-right (resp. top-left to bottom-right) direction staircase with a domain-wall along the top-left to bottom-right (resp. bottom-left to top-right) diagonal to be favoured in the superposition, see Fig. 2 (c). The q and $\frac{1}{q}$ parametrizations are related by a duality transformation of rotating the lattice by $\frac{\pi}{2}$. In the rest of the paper, we shall focus on even N and $q = 1$, for which the ground state thus is the equally-weighted sum of all the (classical) FPL configurations with DWBC1.

To deform the Hamiltonian locally with an even larger class of parameters, we can consider the graph Laplacian that gives the Hamiltonian. That graph turns out to have chordless cycles only of length four, originating from flipping two corner-sharing plaquettes in different orders. The projectors acting on each plaquette p can be deformed in a frustration-free manner independently by a spatially varying angle θ_p not subject to any consistency relation of the type in Ref. [37]: $P_p(\theta_p) = (\cos \theta_p |\uparrow\uparrow\rangle - \sin \theta_p |\uparrow\downarrow\rangle) (\cos \theta_p |\downarrow\uparrow\rangle - \sin \theta_p |\downarrow\downarrow\rangle)_p$.

The necessary and sufficient condition for a boundary configuration allowing an integer energy eigenvalue is most succinctly expressed in the six-vertex language: First, the total number of inward and outward pointing arrows must be the same; in addition, if the lattice is divided along any row or column, the difference between inward and outward pointing arrows on either side of the perimeter can not exceed N . The necessity follows straightforwardly from the conservation of arrows at each vertex, so any partition of the lattice must leave the interior arrows along the cut capable of balancing the net arrow flow in the exterior. The sufficiency condition is proven with backward induction in Appendix B.

An eigenstate with $2n$ flipped boundary spins relative to DWBC1 (in Fig. 2 (c)), and otherwise being annihilated by the bulk Hamiltonian in a construction similar to the ground state, will have energy $E = 2n$. As explained above and proved in Appendix B, a consistent boundary condition in the height representation requires color balancing, meaning that there is a balanced number of covered boundary bonds connected to vertices of either sublattice, i.e. n red and n blue vertices connected to covered boundary bonds. The excited state for a consistent boundary condition \mathcal{S}_n (the set of boundary spins) thus takes the form

$$|2n, \mathcal{S}_n\rangle \propto \sum_{\mathcal{F} \in \text{FPL with } \mathcal{S}_n} |\mathcal{F}\rangle, \quad (9)$$

where the sum runs over FPLs with boundary condition \mathcal{S}_n . A simple estimate for the degeneracy of level $2n$ is $d_{2n} \leq \binom{2N}{n}^2$ since there are $\binom{2N}{n}$ ways in which both

n blue and n red boundary spins can be flipped from DWBC1. This is an upper bound since it includes a handful of boundary configurations violating the second part of the sufficiency condition explained above [49]. For $n = 0$ we recover the unique ground state with $E = 0$ and $\mathcal{S}_0 = \text{DWBC1}$, and for $n = 2N$ we get the unique excited state with $E = 4N$ and $\mathcal{S}_{2N} = \text{DWBC2}$. This $E = 4N$ state is related to the ground state by the \mathbb{Z}_2 operator \mathcal{R} from Eq. (3) and (4).

C. Relation to quantum many-body scars

Here we comment on how our mechanism of weak ergodicity breaking contrasts and complements the known paradigms of spectrum generating algebra [50] and the Shiraishi–Mori embedding formalism [51]. Our Hamiltonian resembles the Shiraishi–Mori formalism, with a target space given by the space of all classical fully packed loops (FPLs). The diagonal boundary Hamiltonian lifts the *a priori* ground state degeneracy, making the ground state unique on the open square grid. Our exact frustration-free excited states are also equidistant in energy. Yet, the majority of our states are not related by ladder operators, except for the ground state and the ceiling state, which are related by the gyration operator [47]. Furthermore, in 2D the contribution of the boundary term to the energy is of order N while the bulk term is of order N^2 , so the exact eigenstates we find do not qualify for QMBS states. The boundary puts stringent constraints on 2D models in constrained Hilbert spaces, to the point that even product state can become eigenstates, which is not observed in 1D, and could lead to potential applications in quantum technology.

IV. BIPARTITE ENTANGLEMENT ENTROPY

The bipartite entanglement entropy of the half-system defined by the central cut shown in Fig. 2 (c) is given by

$$S = - \sum_{\{\vec{m}\}} p_{\vec{m}} \ln p_{\vec{m}}, \quad (10)$$

where $\vec{m} = (h(N/2, 1), h(N/2, 2), \dots, h(N/2, N))$ is the height field across the cut. In what follows we will evaluate this for the ground state using an exact recursion relation.

A. Schmidt decomposition and exact recursion

The numbers $p_{\vec{m}}$ are obtained by Schmidt decomposing the ground state, in analogy with the strategy of Salberger and Korepin [25] in the 1D Fredkin chain:

$$|\text{GS}\rangle = \sum_{\{\vec{m}\}} \sqrt{p_{\vec{m}}} |\mathcal{P}_{L, \vec{m}}(N/2)\rangle \otimes |\mathcal{P}_{R, \vec{m}}(N/2)\rangle, \quad (11)$$

where $|\mathcal{P}_{L, \vec{m}}(N/2)\rangle = \sum_{\mathcal{F} \in \text{FPL with } \vec{m}_R} |\mathcal{F}\rangle$ is the sum of FPLs in the left half-system with height \vec{m} imposed on the right edge (and DWBC on the remaining three), and similarly $|\mathcal{P}_{R, \vec{m}}(N/2)\rangle = \sum_{\mathcal{F} \in \text{FPL with } \vec{m}_L} |\mathcal{F}\rangle$ is the sum of FPLs in the right half with \vec{m} imposed on the left edge. The number of central height field vectors is

$$\mathcal{N}_{\vec{m}} = \binom{N}{N/2}, \quad (12)$$

as obtained by counting Dyck-like paths starting and ending at $h = N/2$ and in increments of $\Delta h = \pm 1$ across neighbouring plaquettes in the central strip. The coefficient $p_{\vec{m}}$ above then takes the form

$$p_{\vec{m}} = \frac{|\mathcal{P}_{L, \vec{m}}(N/2)| |\mathcal{P}_{R, \vec{m}}(N/2)|}{A(N)}, \quad (13)$$

where $|\mathcal{P}_{R, \vec{m}}(N/2)|$ is the number of FPLs in the right half-system with the left boundary \vec{m} . By reflection symmetry around the central cut we have $|\mathcal{P}_{R, \vec{m}}(N/2)| = |\mathcal{P}_{L, \vec{N} - \vec{m}}(N/2)|$, with $\vec{N} = (N, N, \dots, N)$. Closed-form expressions for $|\mathcal{P}_{L, \vec{m}}(N/2)|$ in terms of contour integrals were given in Ref. [52], however, for the purpose of extracting the EE scaling, it is more efficient to use a recurrence relation to enumerate them for incrementally growing N . We refer to Appendix C for details on the recursion relation. [53].

B. Scaling of the entanglement entropy

The combinatoric nature of the counting problem explained above, related to the rapid growth of $A(N)$ [48], and the exponential slowdown encountered when solving the recursion relation numerically still pose as a practical challenge.

In Fig. 6 we show the outcome of calculating the entanglement entropy of the half-system from the exact recursion relation. A Monte Carlo algorithm, which does not rely on ergodicity and which faithfully samples FPL configurations, was devised and verifies the results with excellent accuracy. Details of the Monte Carlo method are provided in Appendix D. The entanglement entropy resulting from the exact recursion relation has area law scaling. Due to the shape of our lattice (having corners) one generally expects subleading corrections like $\ln N$. On the cylinder and torus the general behaviour is a non-universal linear term and a universal constant related to the Lifshitz field theory relevant at the quantum critical point [42, 54, 55].

To shed further light on the scaling we can state a simple upper bound on Eq. (10) in the height field representation. The extreme case is obtained for a flat distribution with $p_{\vec{m}} = 1/\mathcal{N}_{\vec{m}}$:

$$S \leq \ln \mathcal{N}_{\vec{m}} \sim N \ln 2 - \frac{1}{2} \ln N + \frac{1}{2} \ln \frac{2}{\pi}. \quad (14)$$

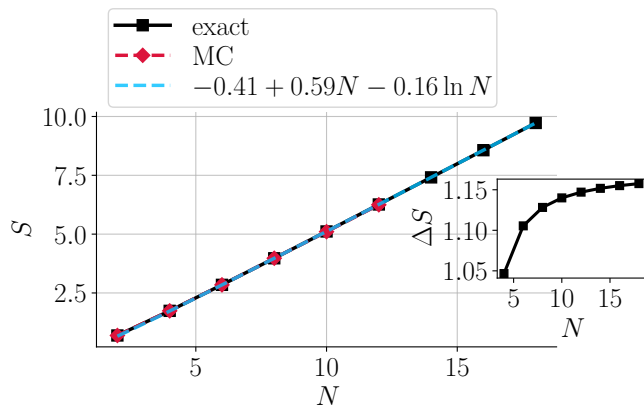


FIG. 6. The bipartite entanglement entropy of the half-system from Eq. (10), as obtained with the exact recursion relation (black squares) described in Appendix C and with the Monte Carlo method (red diamonds) described in Appendix D. The blue dashed line shows a fit to the last three data points. The inset shows the difference between consecutive points, $\Delta S(N) = S(N) - S(N-2)$, which from the upper bound of Eq. (14) is expected to saturate to a constant for large N .

This shows that the growth of the number of central height field configurations is only enough to make the half-system entanglement entropy upper bounded by $N \ln 2$. The same argument applies to the exact excited states, while a generic excited state would not be subjected to the same Schmidt decomposition of Eq. (11) and therefore have EE upper bounded by Lieb’s residue entropy of square ice instead [12]. Recently, a 2D generalization of the Fredkin model was proposed on the hexagonal lattice with the dimer constraint [56]. In Appendix E, we define a similar 2D generalization of the Fredkin spin chain to the square lattice with the FPL constraint. By the logic of the upper bound above this model presumably also faces a ground state bipartite entanglement entropy bounded by area law. The same conclusion is expected to hold for other height-conserving dimer models considered recently [57].

From a tensor network point of view, the ground states of both models can be view as given by projected entangled paired state (PEPS), with virtual legs corresponding to our physical degrees of freedom, and no degrees of freedom on the physical legs. In the tensor network language, the EE scaling is given by the number of bonds crossed by the boundary between subsystems. So to achieve an area law breaking entanglement entropy or a real 2D generalization to the Fredkin model, one may consider constructing a 3D holographic tensor network for which the physical legs only live on the bottom layer, while for the rest of the layers, the virtual leg from the previous layer plays the role of a physical leg [58].

V. UPPER BOUND ON THE SPECTRAL GAP

The classical six-vertex model at the homogeneous point, at which the energies of the a , b , and c vertices are equal, is critical [59], with algebraically decaying bond-bond correlators. By construction, the ground state of our quantum Hamiltonian has the same equal-time correlation function as the classical model, which mean the spectral gap between ground state and first excited state must vanish in the thermodynamic limit [60–63]. In this section, we construct a trial wave function to show that the excitation gap is upper bounded by a quantity that decays exponentially with the system size.

The trial wave function needs to meet two requirements: it has to be both orthogonal to the ground state, and the Hamiltonian must have a expectation value that approaches zero in thermodynamic limit. The first requirement can be satisfied by adding a “twist” to the ground state superposition [24], such that when taking the inner product with the ground state, the two parts with opposite signs cancel. The second requirement calls for a carefully chosen boundary between the two sets of configurations, such that the Hamiltonian annihilates the intra-set contributions, leaving only contributions from the interface of the sets in the energy expectation value. A convenient choice of the set boundary is halfway between the highest $V_{\max} = \frac{1}{3}N(N+1)(2N+1)$ and lowest $V_{\min} = \frac{1}{3}N(N+1)(N+2)$ volume configurations (as found by summing up the configurations in Eq. (D4)). The two sets contain the same number of configurations, and one has to traverse one of the many such configurations to go from configurations with a volume smaller than their average, $V_0 := \frac{1}{2}(V_{\min} + V_{\max}) = \frac{N(N+1)^2}{2}$, to one with a larger volume, see Fig. 7. We thus pick the trial state

$$|\pi\rangle = \sum_{\mathcal{F} \in \text{FPL with DWBC1}} \text{sgn}(V(\mathcal{F}) - V_0) |\mathcal{F}\rangle. \quad (15)$$

It immediately follows that $\langle \text{GS} | \pi \rangle = 0$ and $\langle \pi | \pi \rangle = A(N)$. Before evaluating its energy expectation value, we first count the numbers of configurations near the volume interface V_0 . A representative configuration with volume $V_0 - 1$ is shown in Fig. 7. The flippable plaquettes of this configuration are all located inside a diamond with half the size of the lattice. Outside this diamond the plaquettes are frozen. Inside, every other plaquette is flippable, giving a total number of $M := \frac{N^2}{4}$ flippable plaquettes. Among these there are $\frac{M+1}{2}$ plaquettes with height $\frac{N}{2} - 1$ and $\frac{M-1}{2}$ with height $\frac{N}{2} + 1$ [64]. The number of configurations with volume $V_0 - 1$ can thus be enumerated as

$$\sum_{n=0}^{\frac{M-1}{2}} \binom{\frac{M-1}{2}}{n} \binom{\frac{M+1}{2}}{n} = \binom{M}{\frac{M+1}{2}}, \quad (16)$$

since one can simultaneously flip any number of pairs of plaquettes of heights $\frac{N}{2} - 1$ and $\frac{N}{2} + 1$ from this reference state and remain in vicinity to the volume boundary.

Each of these configurations can be brought across the volume boundary by $\frac{M+1}{2}$ Hamiltonian terms flipping one of the plaquettes with height $\frac{N}{2} - 1$. We have

$$\begin{aligned} \langle \pi | H | \pi \rangle &= \sum_{V(\mathcal{F}), V(\mathcal{F}')=V_0 \pm 1} \langle \mathcal{F} | H | \mathcal{F}' \rangle \\ &= \frac{M+1}{2} \binom{M}{\frac{M+1}{2}}. \end{aligned} \quad (17)$$

Using the asymptotic behaviour of $A(N)$ from Eq. (8) [48] we find

$$\lim_{N \rightarrow \infty} \frac{\langle \pi | H | \pi \rangle}{\langle \pi | \pi \rangle} \sim N^{\frac{41}{36}} \left(\frac{\sqrt[4]{2}}{3\sqrt{3}/4} \right)^{N^2} \rightarrow 0, \quad (18)$$

proving that the Hamiltonian is gapless in the thermodynamic limit.

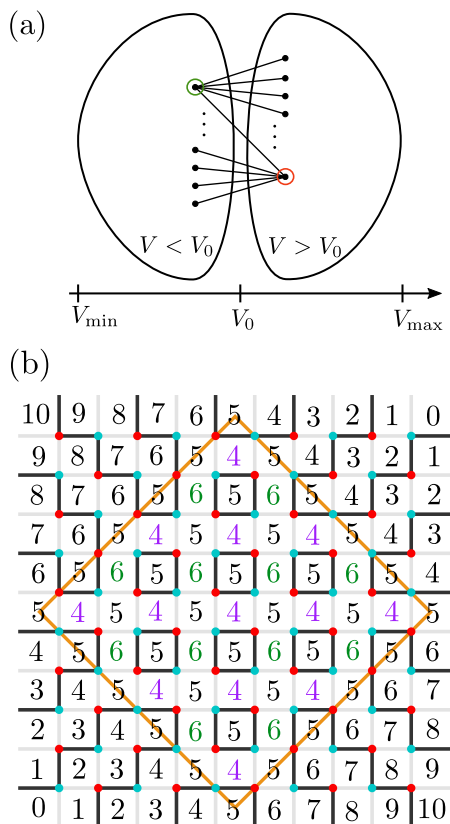


FIG. 7. (a) Fully packed loop configurations with domain-wall boundary conditions partitioned into two sets, dictated by the volume of the configuration. Only configurations in the vicinity of the boundary between the two sets, as measured in a volume metric, contribute to the energy expectation of the trial state in Eq. (15). (b) One of the $\binom{M}{\frac{M+1}{2}}$ configurations (with $M = N^2/4$) with volume $V_0 - 1$. The other configurations are obtained by simultaneously flipping an equal number of plaquettes with height 6 and 4.

VI. CONCLUSIONS

We constructed a quantum fully packed loop model with a Rokhsar–Kivelson type Hamiltonian [45], in which configurations permit multiple equivalent formulations from the classical statistical mechanics and combinatorics literature. By making the model frustration-free the quantum ground state becomes an equal superposition of configurations from the classical space of configurations. We showed that the bulk configurations are heavily constrained by the boundary, to the point that certain boundary configurations imply product eigenstates. The bulk Hamiltonian is not ergodic in the entire Hilbert space, but only within each Krylov subspace, as dictated by the boundary configuration. Each ergodic subspace has its own lowest energy eigenstate, which are equidistant in energy across subspaces. Owing to enumerable half-system configurations by recursion, we performed an exact lattice calculation of the ground state bipartite entanglement entropy for systems of sizes up to 18×18 giving area law scaling.

Our methodology may turn useful in the study of other height models and in related studies of ergodicity breakdown induced by boundary terms. One possible generalization is to consider a \mathbb{Z}_n generalized model involving a boundary condition that alternates with period n instead of two. One may also expect the emergence of interesting phases and refined structures in the Hilbert space fragmentation for fully packed loop models adopted to non-bipartite lattices. Lattices of interest include the triangular one [65–67], or more exotic ones such as the Kagome lattice [68], or even aperiodic tilings like the Penrose [69] and the Ammann–Beenker tiling.

One could attempt to construct a microscopic Hamiltonian that makes the FPL constraint emerge, like what was done for the dimer model in Refs. 70 and 71 using Klein terms of the Hamiltonian. There are also alternative ways to implement the DWBC, for example, by employing an antiferromagnetic interaction along the boundary. The outcome of this choice, other than making the ground state two-fold degenerate and the exact excited states reordered in energy, is that the entire Hamiltonian will have a \mathbb{Z}_2 symmetry.

One can also introduce dynamic terms in the boundary Hamiltonian, so that the fragmentation is removed and the unique ground state becomes the superposition of FPLs with all boundary configurations. It would be of interest to explore the consequences of that on the EE scaling. In addition, it is also interesting to think of whether the Hamiltonian can be modified to reallocate the exact excited states to mid-spectrum QMBS states.

ACKNOWLEDGMENTS

ZZ thanks Filippo Colomo, Hoshio Katsura, Israel Klich, and Jeffrey Teo for fruitful discussions. ZZ acknowledges the kind hospitality of the workshop “Ram-

domness, Integrability and Universality” at the Galileo Galilei Institute for Theoretical Physics during the final stage of this work. HSR acknowledges helpful conversations with Michele Burrello, Paul Fendley, Thomas Scaffidi, Steven H. Simon, Felix Flicker, Olav F. Syljuåsen, and Weronika Wrzos-Kaminska. HSR also thanks Hanne S. Røising for sending Hamiltonian cycle puzzles from the

newspaper per post. ZZ was supported in part by the European Research Council under grant 742104. HSR was supported by a research grant (40509) from VILLUM FONDEN. HSR was also supported by VILLUM FONDEN via the Centre of Excellence for Dirac Materials (Grant No. 11744). We acknowledge the computing resource norlx68 at Nordita. Nordita is partially supported by Nordforsk.

-
- [1] J. M. Deutsch, *Phys. Rev. A* **43**, 2046 (1991).
- [2] M. Srednicki, *Phys. Rev. E* **50**, 888 (1994).
- [3] R. Nandkishore and D. A. Huse, *Annual Review of Condensed Matter Physics* **6**, 15 (2015), <https://doi.org/10.1146/annurev-conmatphys-031214-014726>.
- [4] D. A. Abanin, E. Altman, I. Bloch, and M. Serbyn, *Rev. Mod. Phys.* **91**, 021001 (2019).
- [5] S. Moudgalya, B. A. Bernevig, and N. Regnault, arXiv e-prints , arXiv:2109.00548 (2021), [arXiv:2109.00548 \[cond-mat.str-el\]](https://arxiv.org/abs/2109.00548).
- [6] J. R. Schrieffer and P. A. Wolff, *Phys. Rev.* **149**, 491 (1966).
- [7] S. Bravyi, D. P. DiVincenzo, and D. Loss, *Annals of Physics* **326**, 2793 (2011).
- [8] I. Lesanovsky and H. Katsura, *Phys. Rev. A* **86**, 041601 (2012).
- [9] P. Fendley, K. Sengupta, and S. Sachdev, *Phys. Rev. B* **69**, 075106 (2004).
- [10] C. J. Turner, A. A. Michailidis, D. A. Abanin, M. Serbyn, and Z. Papić, *Nat. Phys.* **14**, 745 (2018).
- [11] H. Bernien, S. Schwartz, A. Keesling, H. Levine, A. Omran, H. Pichler, S. Choi, A. S. Zibrov, M. Endres, M. Greiner, V. Vuletić, and M. D. Lukin, *Nature* **551**, 579 (2017).
- [12] E. H. Lieb, *Phys. Rev.* **162**, 162 (1967).
- [13] G. Kuperberg, arXiv Mathematics e-prints , math/9712207 (1997), [arXiv:math/9712207 \[math.CO\]](https://arxiv.org/abs/math/9712207).
- [14] W. Mills, D. P. Robbins, and H. Rumsey, *Journal of Combinatorial Theory, Series A* **34**, 340 (1983).
- [15] D. Zeilberger, *The Electronic Journal of Combinatorics* **3**, <https://doi.org/10.37236/1271> (1996).
- [16] D. M. Bressoud, *Proofs and Confirmations: The Story of the Alternating-Sign Matrix Conjecture*, Spectrum (Cambridge University Press, 1999).
- [17] P. Schiffer and C. Nisoli, *Applied Physics Letters* **118**, 110501 (2021).
- [18] R. F. Wang, C. Nisoli, R. S. Freitas, J. Li, W. McConville, B. J. Cooley, M. S. Lund, N. Samarth, C. Leighton, V. H. Crespi, and P. Schiffer, *Nature* **439**, 303 (2006).
- [19] U.-J. Wiese, *Annalen der physik* **525**, 777 (2013).
- [20] A. W. Glaetzle, M. Dalmonte, R. Nath, I. Rouschatzakis, R. Moessner, and P. Zoller, *Phys. Rev. X* **4**, 041037 (2014).
- [21] A. Celi, B. Vermersch, O. Viyuela, H. Pichler, M. D. Lukin, and P. Zoller, *Phys. Rev. X* **10**, 021057 (2020).
- [22] G. Semeghini, H. Levine, A. Keesling, S. Ebadi, T. T. Wang, D. Bluvstein, R. Verresen, H. Pichler, M. Kalinowski, R. Samajdar, A. Omran, S. Sachdev, A. Vishwanath, M. Greiner, V. Vuletić, and M. D. Lukin, *Science* **374**, 1242 (2021).
- [23] R. Samajdar, W. W. Ho, H. Pichler, M. D. Lukin, and S. Sachdev, *Proceedings of the National Academy of Sciences* **118**, e2015785118 (2021).
- [24] S. Bravyi, L. Caha, R. Movassagh, D. Nagaj, and P. W. Shor, *Phys. Rev. Lett.* **109**, 207202 (2012).
- [25] O. Salberger and V. Korepin, arXiv e-prints , arXiv:1605.03842 (2016), [arXiv:1605.03842 \[quant-ph\]](https://arxiv.org/abs/1605.03842).
- [26] L. Dell’Anna, *SciPost Phys.* **7**, 53 (2019).
- [27] C. M. Langlett and S. Xu, *Phys. Rev. B* **103**, L220304 (2021).
- [28] J. Richter and A. Pal, *Phys. Rev. Research* **4**, L012003 (2022).
- [29] A. Khudorozhkov, A. Tiwari, C. Chamon, and T. Neupert, arXiv e-prints , arXiv:2107.09690 (2021), [arXiv:2107.09690 \[cond-mat.str-el\]](https://arxiv.org/abs/2107.09690).
- [30] D. N. Page, *Phys. Rev. Lett.* **71**, 1291 (1993).
- [31] M. B. Hastings, *Journal of Statistical Mechanics: Theory and Experiment* **2007**, P08024 (2007).
- [32] A. Anshu, I. Arad, and D. Gosset, arXiv e-prints , arXiv:2103.02492 (2021), [arXiv:2103.02492 \[quant-ph\]](https://arxiv.org/abs/2103.02492).
- [33] J. Eisert, M. Cramer, and M. B. Plenio, *Rev. Mod. Phys.* **82**, 277 (2010).
- [34] P. Calabrese and J. Cardy, *Journal of Physics A: Mathematical and Theoretical* **42**, 504005 (2009).
- [35] D. Goev and I. Klich, *Phys. Rev. Lett.* **96**, 100503 (2006).
- [36] R. Movassagh and P. W. Shor, *Proceedings of the National Academy of Sciences* **113**, 13278 (2016), <https://www.pnas.org/content/113/47/13278.full.pdf>.
- [37] Z. Zhang, A. Ahmadain, and I. Klich, *Proceedings of the National Academy of Sciences* **114**, 5142 (2017), <https://www.pnas.org/content/114/20/5142.full.pdf>.
- [38] O. Salberger, T. Udagawa, Z. Zhang, H. Katsura, I. Klich, and V. Korepin, *Journal of Statistical Mechanics: Theory and Experiment* **2017**, 063103 (2017).
- [39] Z. Zhang and I. Klich, *Journal of Physics A: Mathematical and Theoretical* **50**, 425201 (2017).
- [40] C. L. Henley, *Journal of Statistical Physics* **89**, 483 (1997), [arXiv:cond-mat/9607222 \[cond-mat\]](https://arxiv.org/abs/cond-mat/9607222).
- [41] J. L. Jacobsen and J. Kondev, *Nuclear Physics B* **532**, 635 (1998).
- [42] E. Ardonne, P. Fendley, and E. Fradkin, *Annals of Physics* **310**, 493 (2004).
- [43] C. M. Herdman and K. B. Whaley, *Phys. Rev. B* **87**, 155150 (2013).
- [44] P. Zinn-Justin, arXiv e-prints , arXiv:0901.0665 (2009), [arXiv:0901.0665 \[math-ph\]](https://arxiv.org/abs/0901.0665).
- [45] D. S. Rokhsar and S. A. Kivelson, *Phys. Rev. Lett.* **61**, 2376 (1988).
- [46] Alternating sign matrices are matrices with elements 0, -1 , or $+1$ such that the sum of each column and row is 1,

- and where the $+1$ and -1 elements alternate along rows and columns. The mapping to six-vertex model configurations is obtained by assigning c_1 vertices $+1$, c_2 vertices -1 , and all the remaining four vertices 0 [13, 16].
- [47] B. Wieland, *The Electronic Journal of Combinatorics* **7**, 10.37236/1515 (2000).
- [48] The asymptotics of $A(N)$, using Stirling’s approximation $\ln(N!) \sim N \ln(N) - N + \frac{1}{2} \ln(2\pi N)$, is dictated by $\ln(A(N)) \sim N^2 \ln(3\sqrt{3}/4)$. Including the sub-leading multiplicative correction results in $A(N) \sim N^{-5/36} (3\sqrt{3}/4)^{N^2}$ [72].
- [49] For $N = 6$ for instance, explicit counting results in a total of 2 668 952 consistent boundary modes, whereas the formula $g(N) := \sum_{n=0}^{2N} \binom{2N}{n}^2 = \frac{4^{2N} \Gamma(2N + \frac{1}{2})}{\sqrt{\pi} \Gamma(2N + 1)}$ predicts $g(6) = 2\,704\,156$.
- [50] D. K. Mark, C.-J. Lin, and O. I. Motrunich, *Phys. Rev. B* **101**, 195131 (2020).
- [51] N. Shiraishi and T. Mori, *Phys. Rev. Lett.* **119**, 030601 (2017).
- [52] F. Colomo, G. Di Giulio, and A. G. Pronko, *Nuclear Physics B* **972**, 115535 (2021).
- [53] The enumeration of half-system configurations for a subset of the \vec{m} ’s has been established with available asymptotics, namely those with “U-turn” boundaries [73] and some with certain symmetry constraints [74].
- [54] B. Hsu, M. Mulligan, E. Fradkin, and E.-A. Kim, *Phys. Rev. B* **79**, 115421 (2009).
- [55] E. Fradkin, *Field Theories of Condensed Matter Physics*, 2nd ed. (Cambridge University Press, 2013).
- [56] L. Causer, J. P. Garrahan, and A. Lamacraft, *arXiv e-prints*, arXiv:2202.06989 (2022), arXiv:2202.06989 [cond-mat.stat-mech].
- [57] Z. Yan, Z. Y. Meng, D. A. Huse, and A. Chan, *arXiv e-prints*, arXiv:2204.01740 (2022), arXiv:2204.01740 [cond-mat.str-el].
- [58] R. N. Alexander, A. Ahmadain, Z. Zhang, and I. Klich, *Phys. Rev. B* **100**, 214430 (2019).
- [59] R. Baxter, *Exactly Solved Models in Statistical Mechanics* (Elsevier Science, 2016).
- [60] F. Colomo and A. G. Pronko, *Journal of Statistical Mechanics: Theory and Experiment* **2005**, P05010 (2005).
- [61] F. Colomo and A. G. Pronko, *Theoretical and Mathematical Physics* **171**, 641 (2012).
- [62] E. Granet, L. Budzynski, J. Dubail, and J. L. Jacobsen, *Journal of Statistical Mechanics: Theory and Experiment* **2019**, 013102 (2019).
- [63] P. Belov and N. Reshetikhin, *arXiv e-prints*, arXiv:2012.05182 (2020), arXiv:2012.05182 [cond-mat.stat-mech].
- [64] We have assumed that $N/2$ is odd. For $N/2$ being even, the construction is analogous with slight modifications.
- [65] R. Moessner and S. L. Sondhi, *Phys. Rev. Lett.* **86**, 1881 (2001).
- [66] P. Fendley, R. Moessner, and S. L. Sondhi, *Phys. Rev. B* **66**, 214513 (2002).
- [67] Z. Yan, X. Ran, Y.-C. Wang, R. Samajdar, J. Rong, S. Sachdev, Y. Qi, and Z. Y. Meng, *arXiv e-prints*, arXiv:2205.04472 (2022), arXiv:2205.04472 [cond-mat.str-el].
- [68] G. Misguich, D. Serban, and V. Pasquier, *Phys. Rev. Lett.* **89**, 137202 (2002).
- [69] F. Flicker, S. H. Simon, and S. A. Parameswaran, *Phys. Rev. X* **10**, 011005 (2020).
- [70] J. Cano and P. Fendley, *Phys. Rev. Lett.* **105**, 067205 (2010).
- [71] D. J. Klein, *Journal of Physics A: Mathematical and General* **15**, 661 (1982).
- [72] OEIS Foundation Inc. (2022), Robbins numbers, Entry A005130 in The On-Line Encyclopedia of Integer Sequences (2022), accessed: 02/06/2022.
- [73] P. Bleher and K. Liechty, *arXiv e-prints*, arXiv:1702.01190 (2017), arXiv:1702.01190 [math-ph].
- [74] I. Fischer and M. P. Saikia, *arXiv e-prints*, arXiv:1906.07723 (2019), arXiv:1906.07723 [math.CO].
- [75] N. Ju, *Enumeration of A^λ -ice models and strict Gelfand-Tsetlin patterns*, Honors Thesis, Wellesley College Digital Repository (2016).
- [76] M. Hermele, M. P. A. Fisher, and L. Balents, *Phys. Rev. B* **69**, 064404 (2004).
- [77] M. Kondákor, *Anisotropic quantum six-vertex model on the square lattice*, Bachelor’s thesis, Wigner Research Centre for Physics (2021).
- [78] This recurrence relation was derived in Ref. 75 where the author proved the relation after mapping to equivalent Gelfand–Tsetlin patterns. Here we give a proof directly from the six-vertex degrees of freedom.
- [79] The number of configurations in the ground state superposition is 690 (cf. 42 for the model in Sec. II) and 14 058 234 (cf. 7 436 for the model in Sec. II) for $N = 4$ and $N = 6$, respectively.

Appendix A: Proof of ergodicity within each Krylov subspace specified by a boundary configuration

In this appendix we prove by induction that each Krylov subspace specified by the boundary configuration is ergodic with respect to the bulk Hamiltonian.

For a 2×2 lattice, there are at most two choices of the bulk configuration, differing by the height on the central plaquette, for any fixed boundary configuration. These two are related by the flipping the central plaquette.

Suppose we have proven the ergodicity for a lattice of size $k \times k$ for any fixed boundary configuration, that is, if such a boundary allows multiple bulk configurations, they are all related to each other by sequences of plaquette flips. Then for a lattice of size $(k+1) \times (k+1)$, for which the bottom left corner is a $k \times k$ lattice with established ergodicity, see Fig. 8, we just need to show that any configuration of the newly added strip above the top and to the right with identical bulk configurations, are related to each other.

To show this, we only need to show connectivity of two strip configurations differing only at the height of any single plaquette, because once that is established, configurations differing at multiple places can be connected step by step transitively. If the difference is located in the corner of the strip, then the two configuration are related by

simply flipping the corner plaquette. Otherwise, if the heights differ on a plaquette p_1 next to the right boundary, its neighbors above and below must have the same height h_0 , or there are at least two plaquettes along the strip with different heights between the two strip configurations in question, contradicting our assumption.

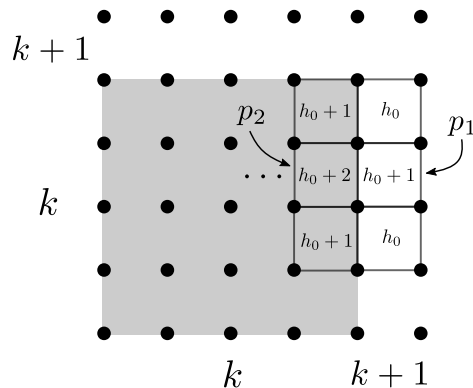


FIG. 8. Proving ergodicity of the bulk Hamiltonian by induction: Two configurations differing only by the height of one plaquette along the strip added in the $(k+1)$ th step are either related by flipping that plaquette, or if it is not flippable, the product of its flipping and the appropriate operations in the $k \times k$ bulk (by its proven ergodicity) makes it flippable.

All we need to do now is to show that there is a bulk configuration in the $k \times k$ sublattice for which the adjacent plaquette p_2 to p_1 has the same height h_0 , then these two otherwise identical bulk configurations are related by flipping plaquette p_1 . And this must be the case, because if not, p_2 must have h_0+2 (resp. h_0-2) if the height on p_1 is h_0+1 (resp. h_0-1), with neighbors above and below both of same height as p_1 , otherwise, the flippability of p_2 implies that there is another bulk configuration with height h_0 on p_2 making p_1 flippable. This argument goes on until we reach at the left boundary, with a monotonic gradient along this row, see Fig. 8. As we established in the exhaustion of product eigenstates, this means the entire lattice must be covered by horizontal straight gradient lines, making the ergodicity proof irrelevant for the boundary configuration under discussion.

In the periodic boundary case, ergodicity was proven in Ref. 76 for the “zero-flux” sector, which contains two configurations with every plaquette flippable, called “ideal states”, and they are connected to each other by flipping half of the plaquettes. Since a global extremum implies a local extremum, each configuration has at least two flippable plaquettes which can be flipped to reduce the difference between maximum and minimum heights until one reaches one of the two ideal states. As elegant as this proof is, it does not work for fixed boundary conditions since the extrema can be located on the boundary. Note that Hilbert fragmentation results in exponentially many subspaces, far more than the number of distinct topological sectors. Modulo exceptions of configurations with no flippable plaquettes, which we provide the precise criteria for in Sec. III A, the ergodicity in other Krylov subspaces under periodic boundary conditions can be proved without too many modifications of the above proof. In Ref. 77, it is stated that the topological sectors are classified by the height change along two perpendicular non-contractible loop directions in the case of periodic boundary conditions. There are N^2 such sectors and the bulk Hamiltonian is ergodic within each of these. Note that this is different from the the case of open boundary conditions considered above, for which the number of sectors is exponentially large.

Finally, ergodicity of plaquette flipping moves among FPLs or dimer coverings is trivial on the hexagonal lattice, but less understood on the (tripartite) triangular lattice [65, 66].

Appendix B: Sufficiency proof of arrow-conservation condition for exact excited states

The fact of zero net inflow of arrows in the six-vertex language for all subsystems of the lattice is sufficient to guarantee exact excited states is proven by construction. We start with an $N \times N$ lattice configuration of which the boundary satisfies this condition, and show how to construct all the configurations of the $(N-1) \times (N-1)$ interior layer that satisfy the same condition. By backwards induction the procedure keeps going until a lattice with only one plaquette is reached, which can be easily shown to allow a consistent configuration by examination. In practice, we use backwards induction in the height degree of freedom.

A boundary configuration for a system of size N satisfying the condition guarantees that heights of plaquettes on opposite sides of the same row or column differ by at most N . We imagine filling in the heights on the plaquettes in the next layer one by one, starting from the plaquette with coordinate $(1, 1)$. If its two neighbors on the left and

below have different heights, then its height is fixed to be the average of those two. Otherwise, if the height difference between plaquette pairs $(1, 0)$, $(1, N + 1)$, and $(0, 1)$, $(N + 1, 1)$ is exactly N , the change must go in the direction of being closer to the height at the end of that row or column. (One can easily check that if the two requirements are simultaneously met one can never run into a contradiction.) In all other cases we have a freedom in choosing the height. Next, we fill in the height of cell $(1, 2)$ in the same way, only this time checking the horizontal constraint of whether height at $(1, 1)$ and $(1, N + 1)$ differ exactly by $N - 1$. After finishing the first row, we fill in the rest of the first column in the same way. Then we proceed to the second last row, checking the height differences at $(1, i)$ and $(N + 1, i)$ instead. And finally, we fill the second last column, checking differences in heights at plaquette $(i, 1)$ and $(i, N + 1)$. In the process, we have guaranteed that the boundary configuration of the $(N - 1) \times (N - 1)$ lattice satisfies the same condition. The induction goes on until the 3×3 lattice, for which we know that the two ends of the middle row and column can differ by at most two, so we can always fill in the height in the center. The resulting height distribution from each outcome of the above procedure would map to a unique FPL configuration, and the exact excited state corresponding to their common boundary configuration is given by the uniform superposition of all of them.

Appendix C: Enumeration of half-system configurations

The recurrence relation for enumerating half-system FPL configurations is most conveniently explained in the language of the six vertices (top row of Fig. 2 (a)) [78]. In this language the height change going one step up increases (resp. decreases) by one if a right (resp. left) pointing arrow is crossed. Due to the boundary condition fixing the height in the middle column to be the same at the top and bottom, half of the arrows pointing left and half pointing right. Along the zeroth column on the left boundary, all arrows are pointing left. If we label the locations of the arrows that are now pointing right instead along the $\frac{N}{2}$ 'th column with a vector $\vec{x} = (x_1, x_2, \dots, x_{N/2})$, then $|\mathcal{P}_{L, \vec{m}}(N/2)|$ in Eq. 11 becomes a function of \vec{x} :

$$\mathcal{P}_{N/2 \times N}(\vec{x}) := |\mathcal{P}_{L, \vec{m}}(N/2)|, \quad (\text{C1})$$

where x_i denotes the location of the i 'th arrow reversed in this column (counting from bottom to top), and $N/2 \times N$ specifies the dimension of the half-system.

For $N = 2$, there is only one allowed configuration for each boundary condition, so $\mathcal{P}_{1 \times 2}(1) = \mathcal{P}_{1 \times 2}(2) = 1$, see Fig. 9 (a). While we only care about right boundary configurations with half of the arrows flipped in the end, in order to enumerate them recursively, we also need the number of configuration with less than half of the arrows flipped. In fact, we also have $\mathcal{P}_{1 \times N}(i) = 1, \forall 1 \leq i \leq N$, corresponding to a kink of vertical arrows on the i 'th row. On the

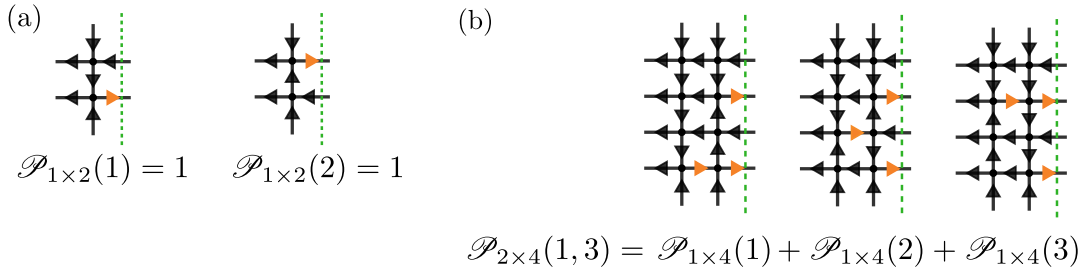


FIG. 9. (a) The two vertex configurations of size 1×2 with kinks of vertical arrows on the first and second row. (b) An illustration of recursively enumerating the configurations of size 2×4 with reversed horizontal arrows on the right boundary on the first and third row, from the counting of configurations of size 1×4 . The orange arrows indicate how each closest pair of right arrows must vertically sandwich a right arrow on their left. The general recursion relation is given by Eq. (C2).

left half-lattice, all the horizontal arrows point to the left along the 0'th column. After taking into account the two inward vertical arrows in the first column at the lower and upper boundary, only one horizontal arrow changes to the right, as there can only be one kink along the vertical line (any more than that would violate the six-vertex rules at some point). Once a horizontal arrow is reversed along the first column, two things can happen after the next column: either it will be reversed to point left again, or one more arrow will be flipped to point right. Only the latter case is relevant to us because, otherwise, we can not accumulate a number of reversed arrows equal to the number of columns $N/2$, which is half of the number of rows, see Fig. 9 (b).

A recurrence relation can be summarized from the simple fact that the right arrows along the previous column must be evenly sandwiched between the rows of each adjacent right arrow pairs in the next column. If instead, all the

horizontal arrows between any two closest right arrows in the next column (including upper and lower boundaries) were pointing to the left, then we would have either an even number of kinks of vertical arrows, or a violation of the six-vertex rules, neither of which is allowed. We have:

$$\mathcal{P}_{(\frac{N}{2}+1) \times (N+2)}(\vec{x}) = \sum_{\substack{x_1 \leq y_1 \leq x_2 \leq y_2 \leq \dots \leq y_{\frac{N}{2}} \leq x_{\frac{N}{2}+1} \\ y_1 \neq y_2 \neq \dots \neq y_{\frac{N}{2}}}} \mathcal{P}_{\frac{N}{2} \times (N+2)}(\vec{y}), \quad (\text{C2})$$

which states that between each neighbouring pairs of reversed horizontal arrows in the current column, there must be one in the previous column, and they must all be distinct.

Appendix D: Monte Carlo method

Here we devise a Monte Carlo method to verify the recursion relation of Appendix C. Given a protocol to generate central height configurations \vec{m} uniformly, the principle is to approximate Eq. (10) as

$$S = - \sum_{\{\vec{m}\}} p_{\vec{m}} \ln p_{\vec{m}} \approx - \sum_{\{\vec{m}\}_{\text{MC}}} \tilde{p}_{\vec{m}} \ln \tilde{p}_{\vec{m}}, \quad (\text{D1})$$

where the distribution $\tilde{p}_{\vec{m}}$ approximates Eq. (13) as

$$\tilde{p}_{\vec{m}} = \frac{M_{\vec{m}} M_{N-\vec{m}}}{M_{\text{MC}}}, \quad (\text{D2})$$

with $M_{\vec{m}}$ being the number of times the central height \vec{m} is sampled, M_{MC} is the total number of configurations sampled, and where $\{\vec{m}\}_{\text{MC}}$ is the set of distinct heights \vec{m} encountered in the M_{MC} samples.

The key part of the algorithm is to uniformly generate the central heights \vec{m} . To achieve this, we iterate row by row from the lower left corner of the graph (with DWBC1 imposed) and draw height configurations with the following rule:

$$h(i, j) = \begin{cases} \frac{1}{2} [h(i-1, j) + h(i, j-1)] & \text{if } h(i-1, j) \neq h(i, j-1) \\ h(i-1, j) - 1 & \text{if } h(i-1, j) = h(i, j-1) \text{ and } h(i-1, j) + 1 > h_{\max}(i, j) \\ h(i-1, j) + 1 & \text{if } h(i-1, j) = h(i, j-1) \text{ and } h(i-1, j) - 1 < h_{\min}(i, j) \\ h(i-1, j) + 1 \text{ with prob. } \frac{1}{2} & \text{if } h(i-1, j) = h(i, j-1) \text{ and } h_{\min}(i, j) < h(i-1, j) < h_{\max}(i, j) \\ h(i-1, j) - 1 \text{ with prob. } \frac{1}{2} & \text{if } h(i-1, j) = h(i, j-1) \text{ and } h_{\min}(i, j) < h(i-1, j) < h_{\max}(i, j) \end{cases}, \quad (\text{D3})$$

where we invoke the globally extremal height configurations, which due to the imposed domain-wall boundary conditions take the form

$$h_{\min}(i, j) = |i - j|, \quad \text{and} \quad h_{\max}(i, j) = \begin{cases} i + j & \text{if } i + j \leq N \\ 2N - i - j & \text{if } i + j > N \end{cases}, \quad (\text{D4})$$

with $h_{\max}(i, j)$ being shown in Fig. 2 (c). To make sure all height configurations are generated with equal probability we trace the number of random numbers drawn to achieve the lower two lines of Eq. (D3), R , and weigh the corresponding branch in the configuration binary tree by 2^R .

In practice the main hurdle to overcome with this algorithm is to make M_{MC} large enough to guarantee that all the $\mathcal{N}_{\vec{m}} \sim 2^N / \sqrt{\pi N/2}$ (Eq. (12)) central heights are encountered with sufficient multiplicity, otherwise accuracy is expected drop and the entropy is eventually underestimated. For instance, with $N = 12$, a single run with $M_{\text{MC}} = 2 \cdot 10^9$ was enough to make $|\{\vec{m}\}_{\text{MC}}| = 922 < 924 = \mathcal{N}_{\vec{m}}$.

Appendix E: A less constrained frustration-free 2D model

One can relax the fixed boundary height and impose the Fredkin moves $|\uparrow\uparrow\downarrow\rangle \leftrightarrow |\uparrow\downarrow\uparrow\rangle$ and $|\downarrow\downarrow\uparrow\rangle \leftrightarrow |\uparrow\downarrow\downarrow\rangle$ in the vertical and horizontal direction by constructing a Hamiltonian made out of projectors onto singlets of Fredkin-flipped states in both the vertical and horizontal direction. Sticking to the bipartite rules of Fig. 2 (a) and (b) we

must distinguish between even and odd plaquettes in doing so, resulting in the Hamiltonian

$$H = \sum_{p \in \{o,e\}} \left[|E_p\rangle \langle E_p| + |W_p\rangle \langle W_p| + |N_p\rangle \langle N_p| + |S_p\rangle \langle S_p| \right], \quad (\text{E1})$$

$$|E_o\rangle = \left| \begin{array}{|c|c|} \hline \cdot & \cdot \\ \hline \cdot & \cdot \\ \hline \end{array} \right\rangle - \left| \begin{array}{|c|c|} \hline \cdot & \cdot \\ \hline \cdot & \cdot \\ \hline \end{array} \right\rangle, \quad |E_e\rangle = \left| \begin{array}{|c|c|} \hline \cdot & \cdot \\ \hline \cdot & \cdot \\ \hline \end{array} \right\rangle - \left| \begin{array}{|c|c|} \hline \cdot & \cdot \\ \hline \cdot & \cdot \\ \hline \end{array} \right\rangle, \quad (\text{E2})$$

$$|W_o\rangle = \left| \begin{array}{|c|c|} \hline \cdot & \cdot \\ \hline \cdot & \cdot \\ \hline \end{array} \right\rangle - \left| \begin{array}{|c|c|} \hline \cdot & \cdot \\ \hline \cdot & \cdot \\ \hline \end{array} \right\rangle, \quad |W_e\rangle = \left| \begin{array}{|c|c|} \hline \cdot & \cdot \\ \hline \cdot & \cdot \\ \hline \end{array} \right\rangle - \left| \begin{array}{|c|c|} \hline \cdot & \cdot \\ \hline \cdot & \cdot \\ \hline \end{array} \right\rangle, \quad (\text{E3})$$

$$|N_o\rangle = \left| \begin{array}{|c|c|} \hline \cdot & \cdot \\ \hline \cdot & \cdot \\ \hline \end{array} \right\rangle - \left| \begin{array}{|c|c|} \hline \cdot & \cdot \\ \hline \cdot & \cdot \\ \hline \end{array} \right\rangle, \quad |N_e\rangle = \left| \begin{array}{|c|c|} \hline \cdot & \cdot \\ \hline \cdot & \cdot \\ \hline \end{array} \right\rangle - \left| \begin{array}{|c|c|} \hline \cdot & \cdot \\ \hline \cdot & \cdot \\ \hline \end{array} \right\rangle, \quad (\text{E4})$$

$$|S_o\rangle = \left| \begin{array}{|c|c|} \hline \cdot & \cdot \\ \hline \cdot & \cdot \\ \hline \end{array} \right\rangle - \left| \begin{array}{|c|c|} \hline \cdot & \cdot \\ \hline \cdot & \cdot \\ \hline \end{array} \right\rangle, \quad |S_e\rangle = \left| \begin{array}{|c|c|} \hline \cdot & \cdot \\ \hline \cdot & \cdot \\ \hline \end{array} \right\rangle - \left| \begin{array}{|c|c|} \hline \cdot & \cdot \\ \hline \cdot & \cdot \\ \hline \end{array} \right\rangle, \quad (\text{E5})$$

In Fig. 10 panel (a) we show the maximal height configuration of this model, and in panel (b) we show the plaquettes that are not flippable in this model, to ensure a positive height. For system sizes of $N = 4, 6$ we confirmed

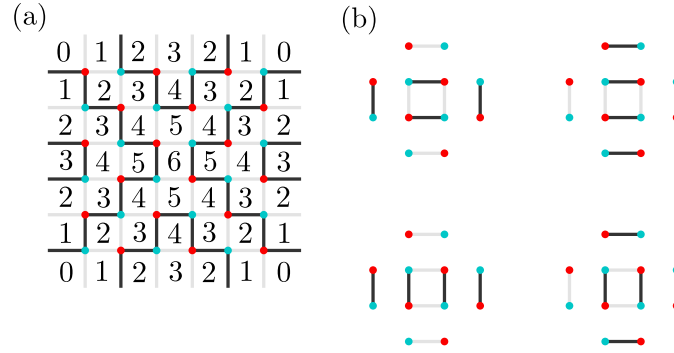


FIG. 10. (a) Maximal height configuration for the model defined in Eq. (E1). (b) The four plaquettes that are not flippable in the model of Eq. (E1) but that are flippable in the quantum dimer model model.

by explicit enumeration [79] that this model exhibits a larger ground state bipartite entanglement entropy than the model of Sec. II. In fact, this is the case for any straight horizontal or vertical system partition. And even though this Hamiltonian poses as a perhaps more direct 2D generalization of the 1D Fredkin chain than Eq. (1), it comes at the price of losing the combinatorial counting technology developed for FPLs with DWBC. And crucially, the simple bound of Eq. (14), or more precisely the growth of the number of height configurations, makes it immediately clear that also this model is bounded by area law bipartite entanglement entropy scaling in the ground state.